Research Square

Preprints are preliminary reports that have not undergone peer review.
They should not be considered conclusive, used to inform clinical practice,
or referenced by the media as validated information.

Structure and substrate selectivity of the lysosomal transporters SLC15A3 and SLC15A4

Tânia Filipa Custódio
European Molecular Biology Laboratory
Siavash Mostafavi
European Molecular Biology Laboratory
Aniket Magarkar
Boehringer Ingelheim Pharma GmbH & Co. KG
Saša Štefanić
University of Zurich
Alexander Pautsch
Boehringer Ingelheim Pharma GmbH & Co. KG
Marc Grundl
Boehringer Ingelheim Pharma GmbH & Co. KG
Christian Löw
christian.loew@embl-hamburg.de

European Molecular Biology Laboratory

Article

Keywords: single particle Cryo-EM, SLC15A3, SLC15A4, transporter, nanobody

Posted Date: November 26th, 2026

DOI: https://doi.org/10.21203/rs.3.rs-11812529/v1

License: This work is licensed under a Creative Commons Attribution 4.0 International License.
Read Full License

Additional Declarations: No competing interests reported.

Abstract

SLC15A3 and SLC15A4 are lysosomal peptide transporters with key roles in innate immunity, where SLC15A4 additionally acts as a scaffold for the adaptor protein TASL to drive type I interferon production downstream of Toll-like receptors. Despite their therapeutic relevance in autoimmune diseases such as systemic lupus erythematosus, the molecular basis of substrate recognition by these lysosomal transporters remains poorly understood. Here we describe NbC4, a conformation-permissive nanobody that enables cryo-EM analysis of monomeric SLC15A4 without restricting TASL binding and use it to determine structures of SLC15A4 bound to two dipeptides, revealing the molecular basis of substrate recognition in the outward-open state. We further capture human SLC15A3 in both outward-open and outward-occluded conformations, providing a structural snapshot of luminal gate closure driven by TM2 bending. A family-wide substrate screen shows that the lysosomal paralogs share a more restricted specificity profile than their plasma membrane counterparts, consistent with differences in binding-site architecture. Together, these findings establish a structural framework for substrate selectivity across the lysosomal SLC15 transporters and lay the groundwork for their selective therapeutic targeting.

Introduction

The solute carrier (SLC) superfamily comprises over 400 membrane transporters grouped into more than 60 families, mediating the translocation of diverse substrates across biological membranes [1–5]. Among them, the SLC15 family, also known as the proton-coupled oligopeptide transporters (POTs), facilitates the uptake of di- and tri-peptides as well as peptide-like drugs by coupling substrate transport to the inward proton gradient [6–12]. The canonical members SLC15A1 (PEPT1) and SLC15A2 (PEPT2) are broadly expressed in the plasma membrane of epithelial tissues and, together with bacterial homologues, have been extensively characterized in terms of substrate specificity, transport mechanism, and structural fold [13–40]. In contrast, the two endolysosomal-resident members, SLC15A3 and SLC15A4, remain much less well understood.

SLC15A3 and SLC15A4 (also termed PHT2 and PHT1, respectively) are primarily expressed in immune cells, localizing to late endosomal and lysosomal membranes where they play key roles in modulating innate immunity and inflammation [41–43]. Both transporters have been reported to mediate proton-dependent uptake of histidine, di- and tri-peptides and peptidoglycan-derived fragments from the lysosomal lumen into the cytoplasm, thereby influencing key immunological pathways such as mTOR signaling, Toll-like receptor (TLR) trafficking, and NOD1/2 activation [44–54].

Dysregulation or genetic disruption of either transporter has been linked to inflammatory and autoimmune disorders including systemic lupus erythematosus and inflammatory bowel disease, underscoring their importance in immune homeostasis [6,55–61]. Beyond transport, both proteins also function as scaffolds in innate immune signaling, though with distinct cell-type distributions and signaling roles. SLC15A4, is predominantly expressed in plasmacytoid dendritic cells and B cells [62–65], where it recruits the adaptor protein TASL (“TLR adaptor interacting with SLC15A4 on the lysosome”) to

activate interferon regulatory factor 5 (IRF5), driving type I interferon responses downstream of endolysosomal TLRs [66,67]. In this context, the transporter activity of SLC15A4 appears dispensable, as lysosomal targeting of TASL alone can restore TLR7–9 signaling [68]. SLC15A3, by contrast, is enriched in macrophages (44–47) and does not directly interact with TASL. Instead, recent evidence suggests it facilitates TASL recruitment to endolysosomes upon TLR7 stimulation, thereby amplifying IRF5-mediated inflammatory signaling [69]. These multifaceted roles make SLC15A3 and SLC15A4 compelling targets for therapeutic modulation of immune responses.

Members of the SLC15 family belong to the Major Facilitator Superfamily (MFS), comprising twelve transmembrane helices organized into two pseudo-symmetrical bundles (N- and C-domains) that operate via an alternating-access mechanism [70,71]. Several recent cryo-EM structures of SLC15A4 have revealed distinct conformations (inward- and outward-open) and oligomeric states (monomeric and dimeric), including complexes with an inhibitor (C5), a natural dipeptide substrate, and the N-terminal region of TASL [13,16,17,38,72]. However, many of these structures relied on conformation-stabilizing fiducial markers, such as synthetic nanobodies or Fab fragments, potentially limiting the conformational landscape accessible for mechanistic and drug discovery studies.

To overcome this limitation, we sought to identify a nanobody that facilitates high-resolution, reproducible cryo-EM analysis of monomeric SLC15A4 without constraining its conformational dynamics. We identified nanobody C4 (NbC4), which binds selectively to one helical bundle of the transporter and is compatible with both outward- and inward-open conformations, as demonstrated by the capture of an outward-open cryo-EM structure and the preserved ability of TASL to bind SLC15A4 in the presence of NbC4. Using this tool, we determined structures of SLC15A4-NbC4 in the apo and dipeptide-bound states, providing molecular insights into substrate recognition. In addition, we resolved the structure of human SLC15A3 bound to a dipeptide and captured multiple conformations within the same dataset. Together with binding assays and molecular dynamics simulations, our findings reveal differences and commonalities between SLC15A3 and SLC15A4 in their substrate-binding pockets, offering a molecular rationale for their partially overlapping but distinct substrate specificities and transport properties. These results establish a mechanistic framework for lysosomal SLC15 transporters and provide a structural foundation for their targeting in immune-mediated diseases.

Results

Cryo-EM structure of SLC15A4 in complex with NbC4

To facilitate the structure determination of chicken SLC15A4 by single-particle cryo-electron microscopy (cryo-EM), we recently generated synthetic nanobodies (“sybodies”) against this transporter. These binders improved particle alignment and enabled high-quality 3D reconstruction [17]. Previous studies have also reported that SLC15A4 can form dimers upon extraction with very mild detergents, a property that was advantageous for cryo-EM analyses [13,38]. However, whether these dimers represent a

physiological relevant state or are simply induced by detergent conditions remains unclear. This dimeric arrangement induces a high membrane curvature and stabilizes the outward-open conformation, not allowing the conformational change to the inward-open conformation and thereby preventing transport.

In our earlier work, we identified sybody 27 (Sb27) as a binder that recognizes two distinct epitopes on SLC15A4 [17]. This dual interaction is mediated by a cholesterol hemisuccinate molecule that is sandwiched between the transporter and the CDR3 loop of Sb27. Although this interaction facilitated structure determination, Sb27 stabilized SLC15A4 in its outward-open conformation, thereby preventing binding of TASL. Consequently, the SLC15A4-Sb27 complex was not suitable for investigating TASL binding or for the development of competitive TASL inhibitors. To overcome this limitation, we sought binders compatible with monomeric SLC15A4 that would both support cryo-EM analyses and permit TASL association. We therefore immunized an alpaca with recombinant SLC15A4 using standard procedures [73] and identified nanobody C4 (NbC4) as a high-affinity binder (Fig. 1). As in our previous study [17], we used chicken SLC15A4, which shares 84% sequence similarity and 77% sequence identity with the human orthologue and yields higher amounts of recombinant protein, while the substrate-binding site residues are fully conserved. NbC4 increased the thermal stability of SLC15A4 by almost 7°C (Fig. 1a) and bound SLC15A4 with an affinity (K_D) of 43 nM (Fig. 1b). In contrast to Sb27, NbC4 neither interfered with TASL peptide binding nor altered its affinity, indicating that NbC4 likely recognizes only one helical bundle of the transporter and does not restrict its conformational cycle between inward- and outward-open states (Fig. 1c.). To map the NbC4 binding interface, we determined the cryo-EM structure of the SLC15A4–NbC4 complex (Fig. 1d, e and Supplementary Fig. 1, 2). The 3D reconstruction reached an overall resolution of 2.93 Å (with local resolution up to 2.6 Å within the transporter core). NbC4 binds exclusively to the luminal side of the N-terminal domain of SLC15A4. The transporter adopts an outward-open conformation, yet NbC4 binding appears to permit the structural flexibility required for transition towards the inward-open state and TASL binding. The overall architecture of the transporter remains highly similar to the previously reported structure, PDB: 8CNI (RMSD = 0.4 Å over 486 C_α atoms) (Supplementary Fig. 2a). Notably, the portion of the loop connecting transmembrane helices 3 and 4 that contacts NbC4 becomes ordered and well-resolved in our reconstruction, whereas this loop was unresolved in prior structures (Fig. 1d, e and Supplementary Fig. 2b, c).

SLC15A4 bound to dipeptides

To date, 15 structural entries for SLC15A4 have been deposited in the Protein Data Bank. These structures capture the transporter in a variety of membrane-mimicking environments, distinct conformational states, and oligomeric forms (monomeric or dimeric). They include complexes with an inhibitor, one natural dipeptide substrate, and an N-terminal TASL fragment [13,16,17,38,72]. Several binding proteins, such as sybodies and Fab fragments, have been developed to stabilize SLC15A4 in defined conformations (either outward-open or inward-open) and to serve as fiducial markers for cryo-EM analysis. NbC4 described here, acts as a fiducial marker without restricting the conformation of the transporter.

To further investigate substrate recognition in this lysosomal peptide transporter, we used the SLC15A4–NbC4 complex and determined cryo-EM structures of the transporter bound to the dipeptides methionine–leucine ('ML') and arginine–phenylalanine ('RF') (Fig. 2 and Supplementary Fig. 2–5). We selected 'ML' because it corresponds to the first two residues of the TASL protein, and 'RF' because it was identified as one of the most stabilizing dipeptides for SLC15A4 in a previous thermostability screen [17]. In addition, the distinctive sidechain features of 'RF' facilitate its unambiguous identification in cryo-EM density maps. A cryo-EM reconstruction of SLC15A4–NbC4 in the presence of high concentrations of histidine (10 mM) did not yield any extra density for histidine nor conformational differences compared to the apo-complex (Supplementary Fig. 5a).

Both dipeptides stabilized SLC15A4 in a concentration-dependent manner, with apparent K_D values of 1.0 mM for 'ML' (Fig. 2c) and 73 µM for the high-affinity peptide 'RF' [17]. Cryo-EM reconstructions of the SLC15A4–NbC4 complex bound to 'RF' and 'ML' were obtained at resolutions of 3.52 Å (Supplementary Fig. 3) and 3.43 Å (Supplementary Fig. 4), respectively. In both cases, the transporter adopts an outward-open substrate-bound conformation. Structural comparison with the apo form (RMSD = 0.4–0.7 Å) revealed only minor local rearrangements (Supplementary Fig. 5b). Additional electron density within the substrate-binding site was clearly attributable to the respective dipeptides, and the coordinating residues could be modeled with high confidence. The positions and conformations of the horizontally bound dipeptides were further validated by 1 µs long molecular dynamics simulations for both systems (Fig. 2h), confirming that the determined structures represent a stable interaction between the transporter and the dipeptides.

The substrate binding pocket is composed of residues from TM1, TM2, TM4 and TM5 in the N-bundle and from TM7, TM8, TM10 and TM11 in the C-bundle. The free amino group of the dipeptide N-terminus is coordinated by a salt bridge with E473 (Fig. 2e and g and Supplementary Fig. 5c and d), consistent with the conserved glutamate that clamps the peptide N-terminus across the SLC15 family and in bacterial POT transporters [19,20,22,24–26,36,37,40]. R44 and K180 are positioned in the vicinity of the dipeptide C-terminal carboxylate (Fig. 2e and g), creating a positively charged electrostatic environment that stabilizes the bound conformation. This asymmetry reflects the architecture of the binding site: E473 is positioned in TM10 of the C-bundle, which forms a pre-organized pocket for the peptide N-terminus, whereas R44 and K180 are localized in TM1 and TM4 of the more mobile N-bundle, which closes in around the C-terminus as the central cavity tightens during the transport cycle [22].

The hydrophobic side-chains at position two of the dipeptides are accommodated in a hydrophobic pocket formed by W340, Y343, F500, F501 and S504, while the side-chains at position one engages with Y207, I210, K180 and T378. The higher affinity of RF relative to ML (73 µM versus 1.0 mM) is explained by two factors: (i) additional hydrogen bonds between the Arg side-chain at position one and T378, contacts entirely absent in the ML-bound structure, and (ii) more extensive hydrophobic burial of the Phe ring at position two within the aromatic pocket formed by W340, Y343, F500, F501 and S504, compared to the smaller Leu side-chain of ML. Overall, the observed interaction patterns are consistent with previous structural and biochemical analyses of other SLC15 members.

Additionally, a thermodynamic water analysis of the molecular dynamics trajectories using SSTMap revealed a conserved, buried hydration site within the SLC15A4 substrate-binding cavity that was retained in both the ML- and RF-bound simulations (Supplementary Fig. 5e). The water molecule occupying this site was energetically favorable, with an estimated energy of approximately − 10 to -12 kcal mol^{-1}, and was stabilized through interactions with S477, Y207, and Y343. In addition to this conserved water site, peptide-specific water-mediated interactions were observed. In the ML-bound complex, a water molecule with an energy of approximately − 16 kcal mol^{-1} formed an extensive network, simultaneously coordinating the peptide N-terminus and the side chains of Q347, D381, and E473 (Supplementary Fig. 5f). A second, partially conserved hydration site was located near R44 / K180 and the peptide C-terminus (approximately − 9 kcal mol^{-1}). In the RF-bound system, an energetically favorable water molecule with an estimated energy of approximately − 15 kcal mol^{-1} mediated an interaction between the Arg side chain and the backbone of T378 and A382 (Supplementary Fig. 5g). Together, these results reveal a combination of conserved protein-coordinated hydration and peptide-specific water-mediated contacts within the SLC15A4 binding cavity, highlighting structured water molecules as integral components of the distinct ML- and RF-binding environments.

Outward-open and outward-occluded structures of human SLC15A3

To investigate structural and potential substrate-binding differences between the lysosomal peptide transporters SLC15A4 and SLC15A3, we expressed and purified detergent-solubilized human SLC15A3 from Expi293F GnTI$^-$ cells, which produce homogeneously glycosylated protein suitable for cryo-EM analysis. In the absence of fiducial markers such as Fabs or nanobodies, we solubilized the transporter in a mild detergent mixture of lauryl maltose neopentyl glycol (LMNG) and CHS. Under this condition we expected a predominately dimeric arrangement as seen for SLC15A4, facilitating improved particle alignment and fiducial-free cryo-EM reconstruction. Initial cryo-EM analyses confirmed that the majority of SLC15A3 particles adopted a dimeric organization in LMNG/CHS, whereas preparations in the commonly used detergent n-dodecyl-β-maltoside (DDM) were mainly monomeric.

We collected single-particle cryo-EM data on dimeric SLC15A3 in the presence of the dipeptide histidine–alanine (‘HA’). During data processing, we observed that the two transporter units within each dimer were asymmetric, allowing classification into two distinct conformations from the same dataset, resulting in two independent reconstructions (Fig. 3 and Supplementary Fig. 6–7). The first reconstruction, refined to 3.6 Å resolution, revealed both protomers in an outward-occluded state (Fig. 3a and Supplementary Fig. 7b), with additional density likely corresponding to the HA dipeptide observed in one protomer. The second reconstruction, at a resolution of 4.0 Å, showed no peptide density; in this structure, one protomer was outward-occluded while the other one adopted a fully outward-open conformation (Fig. 3b and Supplementary Fig. 7a).

To validate the conformational assignments, we superposed all four protomers pairwise. The three outward-occluded protomers superpose with a mean pairwise RMSD of 0.48 Å over 325 C_α atoms,

confirming the consistency of the conformational assignment across both independent reconstructions. The mean RMSD between the occluded and outward-open protomers is 0.67 Å, with the conformational difference localized primarily to TM2 and the luminal gate region (Supplementary Fig. 8a).

The EM map enabled model building from residue 29 at the N-terminus to residue 567 at the C-terminus (of 581 residues in total). Several luminal loops (residues 124–156, 349–371 and 439–454) connecting TM3/TM4, TM7/TM8 and TM9/TM10 were poorly resolved and could not be modeled. Similarly, the bundle bridge (residues 251–307) was only partially resolved. SLC15A3 adopts the canonical MFS fold, comprising an N-terminal bundle (TM1–6) and a C-terminal bundle (TM7–12) connected by a cytoplasmic bundle bridge, consistent with other SLC15 family members. On the luminal side, a short β-hairpin connecting TM9 and TM10, is predicted at the equivalent position of the extracellular domain present in SLC15A1 and SLC15A2, analogous to that observed in SLC15A4.

The outward-open structures of SLC15A3 and SLC15A4 superimpose with an RMSD of 1.9 Å over 321 C_α atoms of the transmembrane core, with the main structural difference being a wider luminal vestibule in SLC15A3 compared to SLC15A4 (Supplementary Fig. 8b). As observed for SLC15A4 [16,38], SLC15A3 dimers adopt a highly curved architecture with additional density at the dimer interface consistent with cholesterol or lipid/detergent molecules, an arrangement that likely prevents a concerted transition to the inward-open state. While each protomer independently adopts functionally relevant conformations, the physiological relevance of the dimeric assembly remains unclear. The outward-occluded structure represents an intermediate state between the outward- and inward-facing states, providing insight into conformational changes during the transport cycle. Structural comparison of the outward-open and outward-occluded SLC15A3 models revealed that rearrangements within the N-terminal bundle, particularly bending of TM2 and to a lesser extent, TM8, drive closure of the luminal gate. This movement is reflected by the decreased distance (from 25 Å to 6 Å) between the tips of TM2 and TM8 (Fig. 3c-e).

Functional and Structural Insights into SLC15A3 dipeptide binding

While the structure and function of the SLC15 family members SLC15A1 and SLC15A2 have been extensively characterized, much less data are available for the lysosomal transporters SLC15A3 and SLC15A4. Compared with SLC15A4, SLC15A3 has been investigated in only a few functional studies [46,50]. Different expression systems and experimental approaches have been employed to characterize this transporter.

To further explore the substrate specificity of SLC15A3 *in vitro*, we examined its binding to a range of di- and tripeptides, as well as other known substrates, using differential scanning fluorimetry (DSF) at two pH values (5.5 and 7.5) [74,75]. Upon substrate binding, the transporter becomes stabilized against heat-induced denaturation, resulting in an increased melting temperature (ΔT_m) (Fig. 4a). The resulting melting profiles indicate that SLC15A3 possesses a broad substrate spectrum, consistent with its role as

a peptide transporter. As expected, SLC15A3 was stabilized by several di- and tripeptides and also by bacterial-derived peptides. Peptides that conferred stabilization at pH 7.5 generally produced a similar effect at pH 5.5. Notably, L-histidine, L-anserine, L-carnosine and the Muramyl Dipeptide (MDP) showed stabilization only at pH 5.5. All four compounds contain a histidine or imidazole moiety, and their selective stabilization at lysosomal pH is consistent with protonation of the imidazole ring enhancing binding under acidic conditions, in line with the lysosomal environment in which SLC15A3 operates. In contrast, peptides containing negatively charged side chains produced little or no stabilization effect, consistent with observations for other SLC15 family members.

For structural studies of SLC15A3, the histidine-containing dipeptide histidine–alanine ('HA') was included in the cryo-EM samples. In the dimeric cryo-EM reconstruction, where both protomers adopt an outward-occluded conformation, one protomer displays an additional density at the expected substrate-binding site, which we assigned to the HA dipeptide (Fig. 4b–c and Supplementary Fig. 9). A concentration-dependent thermal stability assay revealed an apparent binding affinity of 449 ± 108 μM (Fig. 4d). At the resolution of the outward-occluded reconstruction, side-chain assignment in the binding site is limited. Molecular dynamics simulations (1 μs) were therefore used to assess the stability of the modelled binding pose, confirming a stable interaction between SLC15A3 and the 'HA' dipeptide throughout the trajectory (Fig. 4e). The substrate-binding pocket of SLC15A3 is lined by residues from both the N- and C-domains (Fig. 4f and Supplementary Fig. 9c). The histidine side-chain at position one is coordinated by hydrogen bonds with S476 and S503, and is further enclosed by W327, V308, V380 and F499 - all residues of the C-bundle. R46 in the N-bundle forms the primary polar contact with the peptide backbone, with additional hydrophobic interactions from L80, Y203 and N207. E472, the structural equivalent of E473 in SLC15A4, is positioned in the vicinity of the peptide but does not form a discrete hydrogen bond. The peptide therefore engages the pre-organized C-bundle pocket through its position-one side-chain rather than through its N-terminus, while the conserved arginine of the mobile N-bundle provides the only direct backbone contact.

A comparison of the SLC15A3–HA and SLC15A4–ML/RF bound structures reveals that the HA dipeptide adopts an inverted orientation within the binding cavity, with the histidine imidazole ring positioned deep in the pocket and the alanine residue oriented toward the luminal opening (Supplementary Fig. 10a). Despite this difference, the conserved binding site residues of the two paralogs superpose closely (Supplementary Fig. 10b). Binding site plasticity has also been described for bacterial homologues, in which adjustment of the peptide position and movement of binding site residues accommodate diverse substrates [25,26,40]. To compare substrate recognition between the two paralogs quantitatively, we determined apparent binding affinities for six peptides (Supplementary Fig. 10c). SLC15A3 bound five of the six peptides more tightly than SLC15A4, with the strongest differences for 'LL' (4.6 ± 0.7 μM versus 326 ± 29 μM) and 'ML' (18.4 ± 2.0 μM versus 998 ± 77 μM). Since the binding site residues are conserved and superpose closely, these differences likely reflect the conformational dynamics of the transporter rather than substrate coordination itself.

Discussion

The cryo-EM structures presented here provide a framework for understanding substrate recognition in the lysosomal SLC15 transporters. NbC4 was key to obtaining monomeric SLC15A4 structures, and unlike previously described binders that lock the transporter in a defined conformation, it binds exclusively to the N-terminal bundle and leaves TASL binding unaffected, as shown by microscale thermophoresis (MST). Both dipeptides bound to SLC15A4 are recognized through the same conserved elements described for SLC15A1 and SLC15A2: the peptide N-terminus is coordinated by a glutamate residue, while conserved arginine and lysine residues create a positively charged environment around the peptide C-terminus. The side-chain at position two is coordinated by a well characterized hydrophobic pocket [22]. A buried hydration site stabilizes the binding cavity and specific water molecules contribute to the binding of different peptides. For SLC15A3, we determined dimeric structures and captured two conformational states within a single dataset, representing consecutive steps of the transport cycle. The 'HA' dipeptide was resolved in the outward-occluded state. Bending of TM2 closes the luminal gate and reduces the distance between the tips of TM2 and TM8 from 25 Å to 6 Å, consistent with the mechanism described for SLC15A1 and SLC15A2 [22] and in line with the alternating-access mechanism that operates across the MFS. The binding site residues of SLC15A3 and SLC15A4 are conserved and superpose closely, including the hydrophobic pocket, predominately formed by the C-bundle, which accommodates the side-chain at position two of the dipeptide. Despite this, the two transporters differ in apparent affinity for the same peptides. Since substrate coordination alone cannot account for this observation, the difference more likely reflects the conformational dynamics of the transporter or the lack of specific lipids that might be crucial for the transporter function. Consistent with the flexibility of this binding site, the dipeptide 'HA' binds in an inverted orientation relative to the more classical dipeptides bound to SLC15A4, placing the position-one histidine in the pre-organized C-bundle pocket that typically coordinates the peptide N-terminus. The peptide remains engaged with the conserved arginine residue that contributes to backbone recognition, but E472 is not within hydrogen bonding distance to the peptide N-terminus seen in other SLC15 peptide bound structures. These differences extend to the SLC15 family as a whole. To compare substrate preferences across the family, we combined the thermal profiling data for SLC15A1, SLC15A2 and SLC15A4 reported previously [17] with the SLC15A3 data presented here. The ΔT_m values were normalized independently for each transporter on a scale of 0–100, so that each profile reflects the relative preference of that transporter for the peptide library, independent of differences in the absolute magnitude of thermal stabilization (Fig. 5a and Supplementary Fig. 11). Several characteristics of substrate preference emerge from these data. Across all four transporters, peptides carrying a negatively charged side chain produced little or no stabilization, indicating that these peptides bind weakly or not at all. Conversely, peptides with a bulky hydrophobic side chain were among the strongest binders for all four transporters, whereas those with small side chains such as alanine or glycine were poorly bound, in line with the conserved C-bundle hydrophobic pocket that accommodates this position. Beyond these shared features, the transporters differ in how broadly they recognize substrates. SLC15A2 seems to be the least discriminating of the family members, stabilized by nearly the entire peptide library, in line with its role as a high affinity, low capacity

transporter. More generally, the plasma-membrane transporters SLC15A1 and SLC15A2 recognize a broader range of peptides than the lysosomal transporters SLC15A3 and SLC15A4. While the stabilization profiles of SLC15A3 and SLC15A4 look similar, peptides with a positively charged amino acid tend to stabilize SLC15A4 more than SLC15A3. While this global data analysis allows a family wide comparison of the same potential substrates, care should be taken since it only provides information on binding rather than transport properties.

To mediate transport, SLC15 members cycle through the same or similar conformational states, in line with a common alternating-access mechanism. The substrate binds in the outward-open conformation, after which inward movement of the N-bundle and bending of TM2 closes the luminal gate to transition to the outward-occluded state, while the C-bundle remains relatively fixed, with only minor rearrangements (Fig. 5b). The conserved backbone recognition, the shared hydrophobic pocket, and this common gating motion together define the features that unite the SLC15 family, on which the differences in substrate affinity and conformational dynamics between individual members are superimposed.

Materials and Methods

Construct design, expression and purification of SLC15A3 and SLC15A4

The genes encoding full-length chicken SLC15A4 (Gallus gallus; UniProt accession F1NG54) and human SLC15A3 (UniProt accession Q8IY34) were inserted into a pXLG expression vector, in frame with an N-terminal Twin-Strep-II tag followed by an HRV-3C protease cleavage site, as previously described [17]. SLC15A4 carried two point mutations, L12A and L13A, introduced into the N-terminal cytoplasmic tail to promote trafficking of the transporter to the plasma membrane, yielding the SLC15A4 L12A/L13A construct used throughout this study; For SLC15A3, the gene was codon-optimised for expression in HEK cells and with no mutations introduced. Both constructs were transiently expressed in Expi293F GnT1- cells (Thermo Fisher Scientific, Cat.# A39240) by polyethylenimine-mediated transfection, following the transient expression protocol described in detail elsewhere [76]. Cells were harvested by centrifugation and resuspended in 50 mM Tris pH 7.5, 300 mM NaCl and 5% glycerol, supplemented with a protease-inhibitor tablet (Roche), DNaseI and 2 mM MgCl2. SLC15A4 L12A/L13A was solubilized in 1% n-dodecyl-β-D-maltopyranoside (DDM, Anatrace)/0.2% cholesteryl hemisuccinate (CHS, Anatrace) for 1 h at 4°C, and the cleared lysate (~ 110,000 × g, 30 min, 4°C) was bound to Strep-Tactin resin (IBA), washed in the same Tris-based buffer containing 1 mM EDTA and 0.1% DDM/0.01% CHS, and eluted in 20 mM HEPES pH 7.5, 100 mM NaCl, 1 mM EDTA, 0.02% DDM/0.004% CHS and 10 mM desthiobiotin, then further purified by size-exclusion chromatography on a Superdex 200 increase 10/300 GL column (Cytiva) in 20 mM HEPES pH 7.5, 100 mM NaCl, 0.01% DDM/0.002% CHS. SLC15A3 was solubilized in 1.5% lauryl maltose neopentyl glycol (LMNG, Anatrace)/0.3% CHS for 1 h at 4°C, and the cleared lysate (~ 110,000 × g, 30 min, 4°C) was bound to Strep-Tactin resin, washed in the same Tris-based buffer

containing 1 mM EDTA and 0.005% LMNG/0.001% CHS, and eluted in 50 mM HEPES pH 7.5, 200 mM NaCl, 1 mM EDTA, 0.005% LMNG/0.001% CHS and 10 mM desthiobiotin. Eluates were concentrated using a 100-kDa molecular-weight cut-off centrifugal concentrator (Amicon Ultra, Millipore); SLC15A3 was further purified by size-exclusion chromatography on a Superose 6 5/150 GL column (Cytiva) in 20 mM HEPES pH 7.5, 150 mM NaCl, 0.003% LMNG/0.0006% CHS. Further polishing of SLC15A4 L12A/L13A prior to structural studies is described under Single particle Cryo-EM below.

Nanobody selection, expression and purification

To generate nanobodies against chicken SLC15A4, the purified protein was used to immunize an alpaca (Vicugna pacos) on a bi-weekly basis over the course of seven weeks as described elsewhere [77]. Following mRNA extraction and cDNA library preparation from peripheral blood mononuclear cells of the immunized alpaca, VHH-fragments were cloned into a phage display vector. Three rounds of phage display selection were performed to enrich for specific binders, with the third round repeated using a modified direct-coating protocol, achieving sufficient enrichment. Ninety-six ELISA-positive clones were selected for sequencing, identifying a single nanobody family, represented by two clonal variants differing by two amino acids (NbB8 and NbC4); NbC4 is the variant used throughout this study. Binding to the transporters was confirmed using biolayer interferometry. For large scale production, the nanobodies were expressed in *E. coli* BL21 cells, using a PelB N-terminal signal peptide to direct them into the periplasm. After periplasmic extraction, the nanobodies were purified using nickel affinity chromatography, as previously described [21,37,78].

Thermal stability measurements and binding affinity determination

The ability of NbC4 to thermally stabilize SLC15A4 was assessed by nanoDSF, using a Prometheus NT.48 device (NanoTemper Technologies): SLC15A4 was diluted to 3 µM in SEC buffer and mixed with an approximately 1.5-fold molar excess of NbC4 in a final volume of 10 µl, incubated for 20 min at room temperature, and melting scans were recorded from 20 to 95°C at 70% excitation power with a heating rate of 1°C/min.

The same technique was used to determine the binding affinities of SLC15A3 and SLC15A4 to their respective peptide ligands: protein was diluted to a final concentration of 4 µM in SEC buffer and supplied with the respective peptides in a concentration range from approximately 5 µM to 20 mM. Before measurement, the samples were incubated for 30 min at room temperature. Melting scans were performed at a temperature range from 20 to 95°C with a temperature increment of 1°C per minute. Thermal unfolding curves were recorded by measuring the ratio of the tryptophan-fluorescence at 350 nm (F350) and 330 nm (F330). The protein melting temperature (T_m) of a given sample was determined as the inflection point of the thermal unfolding curves, or the local maximum of its first derivative. The measured curves were analysed using the manufacturer's software (PR.ThermControl, v 2.1.2,

NanoTemper Technologies). Based on the determined T_m values, ligand induced thermal shifts (ΔT_m) were determined as the difference between the melting temperature of the ligand-bound state (T_m) and the apo state (T_m^{apo}). For the determination of apparent binding affinities at 25°C, the T_m values recorded from dilution series of the respective ligands were used to fit the following equation:

$$\frac{\Delta T_m}{T_m^{apo}}(L) = \frac{-RT_{std}}{E_{a1}} * \ln\left(\frac{K_{d,app}}{K_{d,app} + L}\right)$$

were L is the ligand concentration, R is the universal gas constant, T_{std} is the chosen standard temperature of 298.15 K (25°C), E_{a1} is the activation energy for the unfolding of the apo state.

As R, T_{std} and L are known and the ΔT_m and T_m^{apo} are experimentally determined, non-linear curve fitting can be used to estimate E_{a1} and $K_{d,app}$. The fitting was performed using symfit (v. 0.5.3), as described in Kotov et al., 2023 [40], based on theoretical considerations formulated in Hall, 2019 [79].

To screen SLC15A3 substrate specificity, a di-/tripeptide and candidate-ligand library was tested at a final concentration of 5 mM against ~ 2 µM SLC15A3 (0.2 mg/ml) at pH 7.5 and pH 5.5. For comparison of substrate profiles across SLC15 family members, ΔT_m values for each transporter were normalised independently to a scale of 0–100, where 0 corresponds to the lowest and 100 to the highest ΔT_m observed for that transporter. This allows comparison of relative substrate preferences between transporters, independent of differences in absolute thermal stabilization. SLC15A4, SLC15A1 and SLC15A2 library-screen data were taken from our previous work [17].

Biolayer interferometry (BLI)

The binding of NbC4 to SLC15A4 was measured by biolayer interferometry (BLI) using the Octet RED96 system (FortéBio). Biotinylated SLC15A4 expressed in ExpiGnT1- cells, was loaded on streptavidin biosensors (FortéBio), pre-equilibrated in 50 mM HEPES, pH 7.5, 200 mM NaCl, 0.02% DDM/ 0.004%CHS supplemented with 0.5% (w/v) BSA, for 20 min. Prior to association, a baseline step of 60 s was performed. Subsequently, sensors were dipped in a two-fold dilution series of NbC4 ranging from 15 to 250 nM for 5 min, followed by an 8 min dissociation step. All experiments were carried out at 22°C. Data were reference-subtracted and aligned to each other in the Octet Data Analysis software (v10.0.3.1, FortéBio), using a global 1:1 binding model. All figures were prepared using Prism 9 (GraphPad).

Microscale Thermophoresis (MST)

SLC15A4 binding to $TASL_{1\text{-}13}$ was assessed by microscale thermophoresis on an MST NT.115 device (NanoTemper Technologies), using a $TASL_{1\text{-}13}$ peptide C-terminally labelled with Cy5 via a PEG spacer. SLC15A4 was serially diluted two-fold in 50 mM HEPES pH 7.5, 100 mM NaCl, 0.02% DDM/0.004% CHS and 10% DMSO, up to a top concentration of 35 µM, and mixed with 25 nM labelled peptide for 10 min at room temperature before loading into standard capillaries. To test competition with NbC4, the same dilution series was pre-incubated for 10 min with 160 µM NbC4 before addition of the labelled peptide.

Measurements used 20% LED and medium MST power, and data were analysed with the MO.Affinity Analysis software (NanoTemper Technologies); figures were prepared in Prism 9 (GraphPad).

Single particle Cryo-EM

Strep-Tactin purified SLC15A4 L12A/L13A expressed in ExpiGnT1- cells was incubated with a two-fold molar excess of NbC4 for 30 min on ice. Just before vitrification, the complex was subjected to a final polishing gel filtration step on a Superose 6 5/150 GL column (Cytiva) in 20 mM HEPES pH 7.5, 100 mM NaCl, 0.003% LMNG/0.0006% CHS. For the dipeptide-bound structures, ML, RF or Histidine was added to a final concentration of 10 mM and the complex was incubated for 1h on ice before grid preparation; For SLC15A3, purified protein was mixed with 10 mM HA dipeptide and incubated for 1h on ice.

For both proteins, samples were applied to glow-discharged Quantifoil 1.2/1.3 Au300 holey-carbon grids at concentrations of 30–45 µM. Grids were blotted and plunge-frozen in liquid ethane/propane mix using a Vitrobot Mark IV (Thermo Fisher Scientific) at 100% humidity and 4°C. Cryo-EM data were collected on Titan Krios microscopes operated at 300 kV and equipped with a Gatan K3 camera in electron-counting mode and a BioQuantum energy filter (slit width 15 eV), using EPU (versions 3.2–3.7, Thermo Fisher Scientific) at a nominal magnification of ×105,000 (pixel size of ~ 0.83 Å) and a total dose of ~ 50 $e^-/Å^2$.

Data processing

Cryo-EM movies for all datasets were processed following the same general pipeline in cryoSPARC v4.5.3 [80], comprising motion correction, CTF estimation, particle picking, 2D and 3D classification, and iterative refinement. For the apo SLC15A4-NbC4 dataset, an initial round of blob picking on the 14,348 collected movies was used to generate templates for a subsequent round of template picking, which yielded 2,337,344 particles. Two rounds of 2D classification resulted in 968,398 particles, followed by three rounds of heterogeneous refinement, leaving 457,750 particles that were refined to 3.04 Å by non-uniform refinement. Local refinement produced a final reconstruction at a global GSFSC resolution of 2.93 Å (Supplementary Fig. 1). For the RF and ML complexes, templates imported directly from the apo dataset were used for template picking, yielding 1,772,727 and 2,806,004 particles, respectively. Two rounds of 2D classification followed by three rounds of heterogeneous refinement yielded 273,777 and 327,451 particles, respectively. The remaining particles from each dataset were subjected to CTF refinement and/or reference-based motion correction, giving reconstructions at 3.64 Å (RF) and 3.49 Å (ML). A final polishing step of local refinement produced final reconstructions at 3.52 Å (RF; Supplementary Fig. 3) and 3.43 Å (ML; Supplementary Fig. 4). For SLC15A3, movies from two data-collection sessions were merged and curated to 18,670 accepted movies (9,747 and 8,923, respectively). As for the SLC15A4-NbC4 datasets, an initial round of blob picking was used to generate templates for a subsequent round of template picking, which yielded 4,904,619 particles. Two rounds of 2D classification selected 1,193,994 particles, followed by two rounds of heterogeneous refinement yielded 181,170 particles, which were refined to 3.7 Å by non-uniform refinement. A round of 3D classification into four classes separated these into two populations - asymmetric dimers with one outward-open and one outward-occluded protomer, and symmetric dimers with both protomers outward-occluded - each of

which was independently refined by non-uniform refinement, followed by local refinement, giving final reconstructions at 4.03 Å (outward-open/outward-occluded) and 3.60 Å (outward-occluded/outward-occluded) (Supplementary Figs. 6–7). Initial models for the SLC15A4-NbC4 structures combined the previously published SLC15A4 coordinates (PDB 8CNI) with an AlphaFold model of NbC4, refined iteratively into each successive dipeptide-bound map; the SLC15A3 structures were built starting from PDB 8WX2. Models were docked into the corresponding maps in ChimeraX [81], then subjected to iterative cycles of manual fitting and correction in Coot [82] and ISOLDE [83], with real-space refinement carried out throughout in Phenix [84]. Model geometry and map-to-model fit were validated with MolProbity [85]. Structural analysis and figure preparation were performed in ChimeraX and PyMOL (Molecular Graphics System, Version 1.5.0.4, Schrödinger, LLC).

Molecular Dynamics Simulations

The initial structural conformation used for molecular dynamics (MD) simulations was obtained from the corresponding experimental structure (PDB ID to be specified). The protein was embedded into a 1,2-dioleoyl-sn-glycero-3-phosphocholine (DOPC) lipid bilayer using the PACKMOL-Memgen workflow in AmberTools 21 [86–89]. Protein parameters were described by the Amber ff99SB-ILDN force field implemented in GROMACS 2021 [90], while lipid parameters were taken from the SLipids force field [91]. The system was solvated using the TIP3P water model [92], and neutralized with sodium and chloride ions to reach a physiological ionic strength of 150 mM.

A hydrogen mass repartitioning (HMR) scheme was applied to enable a 4 fs integration timestep [93,94]. In this approach, hydrogen atom masses, except those in water molecules, were increased to 3 amu. All hydrogen bond constraints were maintained using the LINCS algorithm [95,96]. The simulation temperature was maintained at 300 K, while pressure was set to 1 atm. Pressure coupling was controlled by the Berendsen barostat during equilibration (τ = 1 ps), and subsequently by the Parrinello–Rahman barostat during production runs (τ = 2 ps) [92,93].

A cutoff of 1.0 nm was applied for short-range electrostatics and van der Waals interactions, and long-range electrostatics were treated using the Particle Mesh Ewald (PME) method [97,98]. The prepared systems were energy-minimized prior to equilibration. A five-step equilibration protocol was conducted with gradually reduced positional restraints on protein backbone atoms, non-hydrogen ligand atoms, and lipid headgroups. The force constants applied for these restraints were sequentially 1.5, 2.5, 1.0, 0.5, and 0.1 kcal mol^{-1} $Å^{-2}$.

Following equilibration, production simulations were performed for 1 μs per replicate, with three independent replicas in total. Trajectory analyses were conducted using GROMACS analysis tools [90] and the MDAnalysis Python package [99]. The analysis for water energetics was performed with SSTMAP algorithm [100].

Material Availability

All reagents generated in this study are available from the Lead Contact with a completed Materials Transfer Agreement.

Data Availability

Cryo-EM maps and atomic models have been deposited in the Electron Microscopy Data Bank (EMDB) and the Protein Data Bank (PDB) under the following accession codes: SLC15A4–NbC4 apo, EMD-100803 and PDB 50OE; SLC15A4–NbC4 bound to ML, EMD-100805 and PDB 50OI; SLC15A4–NbC4 bound to RF, EMD-100804 and PDB 50OG; SLC15A3 outward-occluded/outward-occluded bound to HA, EMD-100807 and PDB 50OL; SLC15A3 outward-open/outward-occluded, EMD-100806 and PDB 50OK.

Declarations

Acknowledgements

We thank the Sample Preparation and Characterization facility at EMBL (Hamburg, Germany) and the team of the CryoEM Facility at CSSB for their support, technical assistance and advice. We thank Bjørn Panyella Pedersen and Camilla Gottlieb Andersen (Aarhus University) for hosting T.C. and for support with functional assays. We thank the Nano-antibody Service Facility, University of Zurich, for nanobody generation, and the alpaca Orfeo for immunisation. We thank all group members for fruitful discussions and continuous support on the project.

Conflict of Interest

The authors declare no competing interests.

References

1. Wiedmer, T. *et al.* Metabolic mapping of the human solute carrier superfamily. *Mol Syst Biol* 21, 560–598, doi:10.1038/s44320-025-00106-4(2025).
2. Wolf, G. *et al.* The genetic interaction map of the human solute carrier superfamily. *Mol Syst Biol* 21, 531–559, doi:10.1038/s44320-025-00105-5(2025).
3. Frommelt, F. *et al.* The solute carrier superfamily interactome. *Mol Syst Biol* 21, 632–675, doi:10.1038/s44320-025-00109-1(2025).
4. Goldmann, U. *et al.* Data- and knowledge-derived functional landscape of human solute carriers. *Mol Syst Biol* 21, 599–631, doi:10.1038/s44320-025-00108-2(2025).
5. Gyimesi, G., Tweedie, S., Bruford, E. & Hediger, M. A. The SLC-ome of membrane transport: From molecular discovery to physiology and clinical applications. *Physiol Rev*, doi:10.1152/physrev.00001.2024(2025).
6. Daniel, H., Spanier, B., Kottra, G. & Weitz, D. From bacteria to man: archaic proton-dependent peptide transporters at work. *Physiology (Bethesda)* 21, 93–102, doi:10.1152/physiol.00054.2005(2006).

7. Daniel, H. & Kottra, G. The proton oligopeptide cotransporter family SLC15 in physiology and pharmacology. *Pflugers Arch* 447, 610–618, doi:10.1007/s00424-003-1101-4(2004).
8. Botka, C. W. *et al.* Human proton/oligopeptide transporter (POT) genes: identification of putative human genes using bioinformatics. *AAPS PharmSci* 2, E16, doi:10.1208/ps020216(2000).
9. Minhas, G. S. & Newstead, S. Recent advances in understanding prodrug transport through the SLC15 family of proton-coupled transporters. *Biochem Soc Trans* 48, 337–346, doi:10.1042/BST20180302(2020).
10. Viennois, E., Pujada, A., Zen, J. & Merlin, D. Function, Regulation, and Pathophysiological Relevance of the POT Superfamily, Specifically PepT1 in Inflammatory Bowel Disease. *Compr Physiol* 8, 731–760, doi:10.1002/cphy.c170032(2018).
11. Brandsch, M. Drug transport via the intestinal peptide transporter PepT1. *Curr Opin Pharmacol* 13, 881–887, doi:10.1016/j.coph.2013.08.004(2013).
12. Meredith, D. & Boyd, C. A. Structure and function of eukaryotic peptide transporters. *Cell Mol Life Sci* 57, 754–778, doi:10.1007/s000180050040(2000).
13. Boeszoermenyi, A. *et al.* A conformation-locking inhibitor of SLC15A4 with TASL proteostatic anti-inflammatory activity. *Nat Commun* 14, 6626, doi:10.1038/s41467-023-42070-3(2023).
14. Boggavarapu, R., Jeckelmann, J. M., Harder, D., Ucurum, Z. & Fotiadis, D. Role of electrostatic interactions for ligand recognition and specificity of peptide transporters. *BMC Biol* 13, 58, doi:10.1186/s12915-015-0167-8(2015).
15. Casagrande, F. *et al.* Projection structure of DtpD (YbgH), a prokaryotic member of the peptide transporter family. *J Mol Biol* 394, 708–717, doi:10.1016/j.jmb.2009.09.048(2009).
16. Chen, X. *et al.* Structural basis for recruitment of TASL by SLC15A4 in human endolysosomal TLR signaling. *Nat Commun* 14, 6627, doi:10.1038/s41467-023-42210-9(2023).
17. Custodio, T. F. *et al.* Molecular basis of TASL recruitment by the peptide/histidine transporter 1, PHT1. *Nat Commun* 14, 5696, doi:10.1038/s41467-023-41420-5(2023).
18. Doki, S. *et al.* Structural basis for dynamic mechanism of proton-coupled symport by the peptide transporter POT. *Proc Natl Acad Sci U S A* 110, 11343–11348, doi:10.1073/pnas.1301079110(2013).
19. Guettou, F. *et al.* Selectivity mechanism of a bacterial homolog of the human drug-peptide transporters PepT1 and PepT2. *Nat Struct Mol Biol* 21, 728–731, doi:10.1038/nsmb.2860(2014).
20. Guettou, F. *et al.* Structural insights into substrate recognition in proton-dependent oligopeptide transporters. *EMBO Rep* 14, 804–810, doi:10.1038/embor.2013.107(2013).
21. Killer, M. *et al.* Cryo-EM Structure of an Atypical Proton-Coupled Peptide Transporter: Di- and Tripeptide Permease C. *Front Mol Biosci* 9, 917725, doi:10.3389/fmolb.2022.917725(2022).
22. Killer, M., Wald, J., Pieprzyk, J., Marlovits, T. C. & Low, C. Structural snapshots of human PepT1 and PepT2 reveal mechanistic insights into substrate and drug transport across epithelial membranes. *Sci Adv* 7, eabk3259, doi:10.1126/sciadv.abk3259(2021).

23. Lichtinger, S. M., Parker, J. L., Newstead, S. & Biggin, P. C. The mechanism of mammalian proton-coupled peptide transporters. *Elife* 13, doi:10.7554/eLife.96507(2024).
24. Lyons, J. A. *et al.* Structural basis for polyspecificity in the POT family of proton-coupled oligopeptide transporters. *EMBO Rep* 15, 886–893, doi:10.15252/embr.201338403(2014).
25. Martinez Molledo, M., Quistgaard, E. M., Flayhan, A., Pieprzyk, J. & Low, C. Multispecific Substrate Recognition in a Proton-Dependent Oligopeptide Transporter. *Structure* 26, 467–476 e464, doi:10.1016/j.str.2018.01.005(2018).
26. Martinez Molledo, M., Quistgaard, E. M. & Low, C. Tripeptide binding in a proton-dependent oligopeptide transporter. *FEBS Lett* 592, 3239–3247, doi:10.1002/1873-3468.13246(2018).
27. Minhas, G. S. *et al.* Structural basis of malodour precursor transport in the human axilla. *Elife* 7, doi:10.7554/eLife.34995(2018).
28. Newstead, S. Recent advances in understanding proton coupled peptide transport via the POT family. *Curr Opin Struct Biol* 45, 17–24, doi:10.1016/j.sbi.2016.10.018(2017).
29. Newstead, S. *et al.* Crystal structure of a prokaryotic homologue of the mammalian oligopeptide-proton symporters, PepT1 and PepT2. *EMBO J* 30, 417–426, doi:10.1038/emboj.2010.309(2011).
30. Parker, J. L. *et al.* Structural basis for antibiotic transport and inhibition in PepT2. *Nat Commun* 15, 8755, doi:10.1038/s41467-024-53096-6(2024).
31. Parker, J. L. *et al.* Cryo-EM structure of PepT2 reveals structural basis for proton-coupled peptide and prodrug transport in mammals. *Sci Adv* 7, doi:10.1126/sciadv.abh3355(2021).
32. Parker, J. L. *et al.* Proton movement and coupling in the POT family of peptide transporters. *Proc Natl Acad Sci U S A* 114, 13182–13187, doi:10.1073/pnas.1710727114(2017).
33. Parker, J. L., Mindell, J. A. & Newstead, S. Thermodynamic evidence for a dual transport mechanism in a POT peptide transporter. *Elife* 3, doi:10.7554/eLife.04273(2014).
34. Quistgaard, E. M., Martinez Molledo, M. & Low, C. Structure determination of a major facilitator peptide transporter: Inward facing PepTSt from Streptococcus thermophilus crystallized in space group P3121. *PLoS One* 12, e0173126, doi:10.1371/journal.pone.0173126(2017).
35. Solcan, N. *et al.* Alternating access mechanism in the POT family of oligopeptide transporters. *EMBO J* 31, 3411–3421, doi:10.1038/emboj.2012.157(2012).
36. Stauffer, M. *et al.* Peptide transporter structure reveals binding and action mechanism of a potent PEPT1 and PEPT2 inhibitor. *Commun Chem* 5, 23, doi:10.1038/s42004-022-00636-0(2022).
37. Ural-Blimke, Y. *et al.* Structure of Prototypic Peptide Transporter DtpA from E. coli in Complex with Valganciclovir Provides Insights into Drug Binding of Human PepT1. *J Am Chem Soc* 141, 2404–2412, doi:10.1021/jacs.8b11343(2019).
38. Zhang, Z. *et al.*The structures of the peptide transporters SLC15A3 and SLC15A4 reveal the recognition mechanisms for substrate and TASL. *Structure*33, 330–337 e334, doi:10.1016/j.str.2024.11.019(2025).

39. Zhao, Y. *et al.* Crystal structure of the E. coli peptide transporter YbgH. *Structure* 22, 1152–1160, doi:10.1016/j.str.2014.06.008(2014).
40. Kotov, V. *et al.* Plasticity of the binding pocket in peptide transporters underpins promiscuous substrate recognition. *Cell Rep* 42, 112831, doi:10.1016/j.celrep.2023.112831(2023).
41. Dong, M., Li, P., Luo, J., Chen, B. & Jiang, H. Oligopeptide/Histidine Transporter PHT1 and PHT2 - Function, Regulation, and Pathophysiological Implications Specifically in Immunoregulation. *Pharm Res* 40, 2585–2596, doi:10.1007/s11095-023-03589-8(2023).
42. He, L. *et al.*The Solute Carrier Transporter SLC15A3 Participates in Antiviral Innate Immune Responses against Herpes Simplex Virus-1. *J Immunol Res* 2018, 5214187, doi:10.1155/2018/5214187(2018).
43. Nakamura, N. *et al.* Endosomes are specialized platforms for bacterial sensing and NOD2 signalling. *Nature* 509, 240–244, doi:10.1038/nature13133(2014).
44. Hu, Y., Song, F., Jiang, H., Nunez, G. & Smith, D. E. SLC15A2 and SLC15A4 Mediate the Transport of Bacterially Derived Di/Tripeptides To Enhance the Nucleotide-Binding Oligomerization Domain-Dependent Immune Response in Mouse Bone Marrow-Derived Macrophages. *J Immunol* 201, 652–662, doi:10.4049/jimmunol.1800210(2018).
45. Song, F. *et al.* Regulation and biological role of the peptide/histidine transporter SLC15A3 in Toll-like receptor-mediated inflammatory responses in macrophage. *Cell Death Dis* 9, 770, doi:10.1038/s41419-018-0809-1(2018).
46. Song, F., Hu, Y., Wang, Y., Smith, D. E. & Jiang, H. Functional Characterization of Human Peptide/Histidine Transporter 1 in Stably Transfected MDCK Cells. *Mol Pharm* 15, 385–393, doi:10.1021/acs.molpharmaceut.7b00728(2018).
47. Bhardwaj, R. K., Herrera-Ruiz, D., Eltoukhy, N., Saad, M. & Knipp, G. T. The functional evaluation of human peptide/histidine transporter 1 (hPHT1) in transiently transfected COS-7 cells. *Eur J Pharm Sci* 27, 533–542, doi:10.1016/j.ejps.2005.09.014(2006).
48. Wang, X. X., Hu, Y., Keep, R. F., Toyama-Sorimachi, N. & Smith, D. E. A novel role for PHT1 in the disposition of l-histidine in brain: In vitro slice and in vivo pharmacokinetic studies in wildtype and Pht1 null mice. *Biochem Pharmacol* 124, 94–102, doi:10.1016/j.bcp.2016.11.012(2017).
49. Sasawatari, S. *et al.* The solute carrier family 15A4 regulates TLR9 and NOD1 functions in the innate immune system and promotes colitis in mice. *Gastroenterology* 140, 1513–1525, doi:10.1053/j.gastro.2011.01.041(2011).
50. Wang, Y. *et al.* Substrate Transport Properties of the Human Peptide/Histidine Transporter PHT2 in Transfected MDCK Cells. *J Pharm Sci* 108, 3416–3424, doi:10.1016/j.xphs.2019.06.016(2019).
51. Wang, Y. *et al.* Expression and regulation of proton-coupled oligopeptide transporters in colonic tissue and immune cells of mice. *Biochem Pharmacol* 148, 163–173, doi:10.1016/j.bcp.2017.12.025(2018).
52. Kobayashi, T. *et al.* Human SLC15A4 is crucial for TLR-mediated type I interferon production and mitochondrial integrity. *Int Immunol* 33, 399–406, doi:10.1093/intimm/dxab006(2021).

53. Kobayashi, T. *et al.* The histidine transporter SLC15A4 coordinates mTOR-dependent inflammatory responses and pathogenic antibody production. *Immunity* 41, 375–388, doi:10.1016/j.immuni.2014.08.011(2014).
54. Damme, M., Guelle, O., Low, C. & Gasnier, B. Roles of lysosomal small-molecule transporters in metabolism and signaling. *Trends Cell Biol* 36, 392–403, doi:10.1016/j.tcb.2025.09.004(2026).
55. Lee, J. *et al.* pH-dependent internalization of muramyl peptides from early endosomes enables Nod1 and Nod2 signaling. *J Biol Chem* 284, 23818–23829, doi:10.1074/jbc.M109.033670(2009).
56. Toyama-Sorimachi, N. & Kobayashi, T. Lysosomal amino acid transporters as key players in inflammatory diseases. *Int Immunol* 33, 853–858, doi:10.1093/intimm/dxab069(2021).
57. Kobayashi, T. & Toyama-Sorimachi, N. Metabolic control from the endolysosome: lysosome-resident amino acid transporters open novel therapeutic possibilities. *Front Immunol* 14, 1243104, doi:10.3389/fimmu.2023.1243104(2023).
58. Bentham, J. *et al.* Genetic association analyses implicate aberrant regulation of innate and adaptive immunity genes in the pathogenesis of systemic lupus erythematosus. *Nat Genet* 47, 1457–1464, doi:10.1038/ng.3434(2015).
59. Han, J. W. *et al.* Genome-wide association study in a Chinese Han population identifies nine new susceptibility loci for systemic lupus erythematosus. *Nat Genet* 41, 1234–1237, doi:10.1038/ng.472(2009).
60. Odhams, C. A. *et al.* Interferon inducible X-linked gene CXorf21 may contribute to sexual dimorphism in Systemic Lupus Erythematosus. *Nat Commun* 10, 2164, doi:10.1038/s41467-019-10106-2(2019).
61. Katewa, A. *et al.* The peptide symporter SLC15a4 is essential for the development of systemic lupus erythematosus in murine models. *PLoS One* 16, e0244439, doi:10.1371/journal.pone.0244439(2021).
62. Baccala, R. *et al.* Essential requirement for IRF8 and SLC15A4 implicates plasmacytoid dendritic cells in the pathogenesis of lupus. *Proc Natl Acad Sci U S A* 110, 2940–2945, doi:10.1073/pnas.1222798110(2013).
63. Blasius, A. L. *et al.* Slc15a4, AP-3, and Hermansky-Pudlak syndrome proteins are required for Toll-like receptor signaling in plasmacytoid dendritic cells. *Proc Natl Acad Sci U S A* 107, 19973–19978, doi:10.1073/pnas.1014051107(2010).
64. Sakata, K. *et al.* Cloning of a lymphatic peptide/histidine transporter. *Biochem J* 356, 53–60, doi:10.1042/0264-6021:3560053(2001).
65. Sreedharan, S., Stephansson, O., Schioth, H. B. & Fredriksson, R. Long evolutionary conservation and considerable tissue specificity of several atypical solute carrier transporters. *Gene* 478, 11–18, doi:10.1016/j.gene.2010.10.011(2011).
66. Heinz, L. X. *et al.* TASL is the SLC15A4-associated adaptor for IRF5 activation by TLR7-9. *Nature* 581, 316–322, doi:10.1038/s41586-020-2282-0(2020).
67. Drobek, A. *et al.* The TLR7/9 adaptors TASL and TASL2 mediate IRF5-dependent antiviral responses and autoimmunity in mouse. *Nat Commun* 16, 967, doi:10.1038/s41467-024-55692-y(2025).

68. Zhang, H. *et al.* SLC15A4 controls endolysosomal TLR7-9 responses by recruiting the innate immune adaptor TASL. *Cell Rep* 42, 112916, doi:10.1016/j.celrep.2023.112916(2023).
69. Huang, T. *et al.* METTL3/ALKBH5-Mediated N6-Methyladenosine Modification Drives Macrophage M1 Polarization via the SLC15A3-TASL-IRF5 Signaling Axis in Psoriasis. *Adv Sci (Weinh)* 12, e01408, doi:10.1002/advs.202501408(2025).
70. Drew, D., North, R. A., Nagarathinam, K. & Tanabe, M. Structures and General Transport Mechanisms by the Major Facilitator Superfamily (MFS). *Chem Rev* 121, 5289–5335, doi:10.1021/acs.chemrev.0c00983(2021).
71. Quistgaard, E. M., Low, C., Guettou, F. & Nordlund, P. Understanding transport by the major facilitator superfamily (MFS): structures pave the way. *Nat Rev Mol Cell Biol* 17, 123–132, doi:10.1038/nrm.2015.25(2016).
72. Zhu, Y. *et al.* Development of conformation-selective antibodies targeting human SLC15A4. *Nat Commun* 16, 7324, doi:10.1038/s41467-025-62759-x(2025).
73. Pardon, E. *et al.* A general protocol for the generation of Nanobodies for structural biology. *Nat Protoc* 9, 674–693, doi:10.1038/nprot.2014.039(2014).
74. Kotov, V. *et al.* In-depth interrogation of protein thermal unfolding data with MoltenProt. *Protein Sci* 30, 201–217, doi:10.1002/pro.3986(2021).
75. Kotov, V. *et al.* High-throughput stability screening for detergent-solubilized membrane proteins. *Sci Rep* 9, 10379, doi:10.1038/s41598-019-46686-8(2019).
76. Custodio, T. F., Guedez, G. & Low, C. Transient Co-expression of Membrane Protein Complexes in Mammalian Cells. *Methods Mol Biol* 2810, 11–28, doi:10.1007/978-1-0716-3878-1_2(2024).
77. Maass, D. R., Sepulveda, J., Pernthaner, A. & Shoemaker, C. B. Alpaca (Lama pacos) as a convenient source of recombinant camelid heavy chain antibodies (VHHs). *J Immunol Methods* 324, 13–25, doi:10.1016/j.jim.2007.04.008(2007).
78. Gabriel, F. *et al.* Structural basis of thiamine transport and drug recognition by SLC19A3. *Nat Commun* 15, 8542, doi:10.1038/s41467-024-52872-8(2024).
79. Hall, J. A simple model for determining affinity from irreversible thermal shifts. *Protein Sci* 28, 1880–1887, doi:10.1002/pro.3701(2019).
80. Punjani, A., Rubinstein, J. L., Fleet, D. J. & Brubaker, M. A. cryoSPARC: algorithms for rapid unsupervised cryo-EM structure determination. *Nat Methods* 14, 290–296, doi:10.1038/nmeth.4169(2017).
81. Pettersen, E. F. *et al.* UCSF ChimeraX: Structure visualization for researchers, educators, and developers. *Protein Sci* 30, 70–82, doi:10.1002/pro.3943(2021).
82. Emsley, P., Lohkamp, B., Scott, W. G. & Cowtan, K. Features and development of Coot. *Acta Crystallogr D Biol Crystallogr* 66, 486–501, doi:10.1107/S0907444910007493(2010).
83. Croll, T. I. ISOLDE: a physically realistic environment for model building into low-resolution electron-density maps. *Acta Crystallogr D Struct Biol* 74, 519–530, doi:10.1107/S2059798318002425(2018).

84. Afonine, P. V. *et al.* Real-space refinement in PHENIX for cryo-EM and crystallography. *Acta Crystallogr D Struct Biol* 74, 531–544, doi:10.1107/S2059798318006551(2018).
85. Williams, C. J. *et al.* MolProbity: More and better reference data for improved all-atom structure validation. *Protein Sci* 27, 293–315, doi:10.1002/pro.3330(2018).
86. Kroon, P. C. *et al.* Martinize2 and Vermouth provide a unified framework for molecular topology generation. *Elife* 12, doi:10.7554/eLife.90627(2025).
87. Wassenaar, T. A., Ingolfsson, H. I., Bockmann, R. A., Tieleman, D. P. & Marrink, S. J. Computational Lipidomics with insane: A Versatile Tool for Generating Custom Membranes for Molecular Simulations. *J Chem Theory Comput* 11, 2144–2155, doi:10.1021/acs.jctc.5b00209(2015).
88. Schott-Verdugo, S. & Gohlke, H. PACKMOL-Memgen: A Simple-To-Use, Generalized Workflow for Membrane-Protein-Lipid-Bilayer System Building. *J Chem Inf Model* 59, 2522–2528, doi:10.1021/acs.jcim.9b00269(2019).
89. Boothroyd, S. *et al.* Development and Benchmarking of Open Force Field 2.0.0: The Sage Small Molecule Force Field. *J Chem Theory Comput* 19, 3251–3275, doi:10.1021/acs.jctc.3c00039(2023).
90. Abraham, M. J. *et al.* GROMACS: High performance molecular simulations through multi-level parallelism from laptops to supercomputers. *SoftwareX* 1–2, 19–25, doi:10.1016/j.softx.2015.06.001(2015).
91. Jambeck, J. P. & Lyubartsev, A. P. Derivation and systematic validation of a refined all-atom force field for phosphatidylcholine lipids. *J Phys Chem B* 116, 3164–3179, doi:10.1021/jp212503e(2012).
92. Jorgensen, W. L., Chandrasekhar, J., Madura, J. D., Impey, R. W. & Klein, M. L. Comparison of Simple Potential Functions for Simulating Liquid Water. *Journal of Chemical Physics* 79, 926–935, doi:10.1063/1.445869(1983).
93. Feenstra, K. A., Hess, B. & Berendsen, H. J. C. Improving efficiency of large time-scale molecular dynamics simulations of hydrogen-rich systems. *J Comput Chem*20, 786–798, doi:10.1002/(SICI)1096-987X(199906)20:8<786::AID-JCC5>3.0.CO;2-B (1999).
94. Hopkins, C. W., Le Grand, S., Walker, R. C. & Roitberg, A. E. Long-Time-Step Molecular Dynamics through Hydrogen Mass Repartitioning. *J Chem Theory Comput* 11, 1864–1874, doi:10.1021/ct5010406(2015).
95. Hess, B., Bekker, H., Berendsen, H. J. C. & Fraaije, J. G. E. M. LINCS: A linear constraint solver for molecular simulations. *Journal of Computational Chemistry* 18, 1463–1472, doi:10.1002/(sici)1096-987x(199709)18:12%3C1463::Aid-jcc4%3E3.0.Co;2-h(1997).
96. Hess, B. P-LINCS: A Parallel Linear Constraint Solver for Molecular Simulation. *J Chem Theory Comput* 4, 116–122, doi:10.1021/ct700200b(2008).
97. Essmann, U. *et al.* A smooth particle mesh Ewald method. *The Journal of Chemical Physics* 103, 8577–8593, doi:10.1063/1.470117(1995).
98. Darden, T., Pearlman, D. & Pedersen, L. G. Ionic charging free energies: Spherical versus periodic boundary conditions. *The Journal of Chemical Physics* 109, 10921–10935, doi:10.1063/1.477788(1998).

99. Gowers, R. J. *et al.*MDAnalysis: A Python Package for the Rapid Analysis of Molecular Dynamics Simulations. *Proc. 15th Python Sci. Conf*, 98–105 doi:10.25080/Majora-629e541a-00e(2016).

100. Haider, K., Cruz, A., Ramsey, S., Gilson, M. K. & Kurtzman, T. Solvation Structure and Thermodynamic Mapping (SSTMap): An Open-Source, Flexible Package for the Analysis of Water in Molecular Dynamics Trajectories. *J Chem Theory Comput* 14, 418–425, doi:10.1021/acs.jctc.7b00592(2018).

Figures

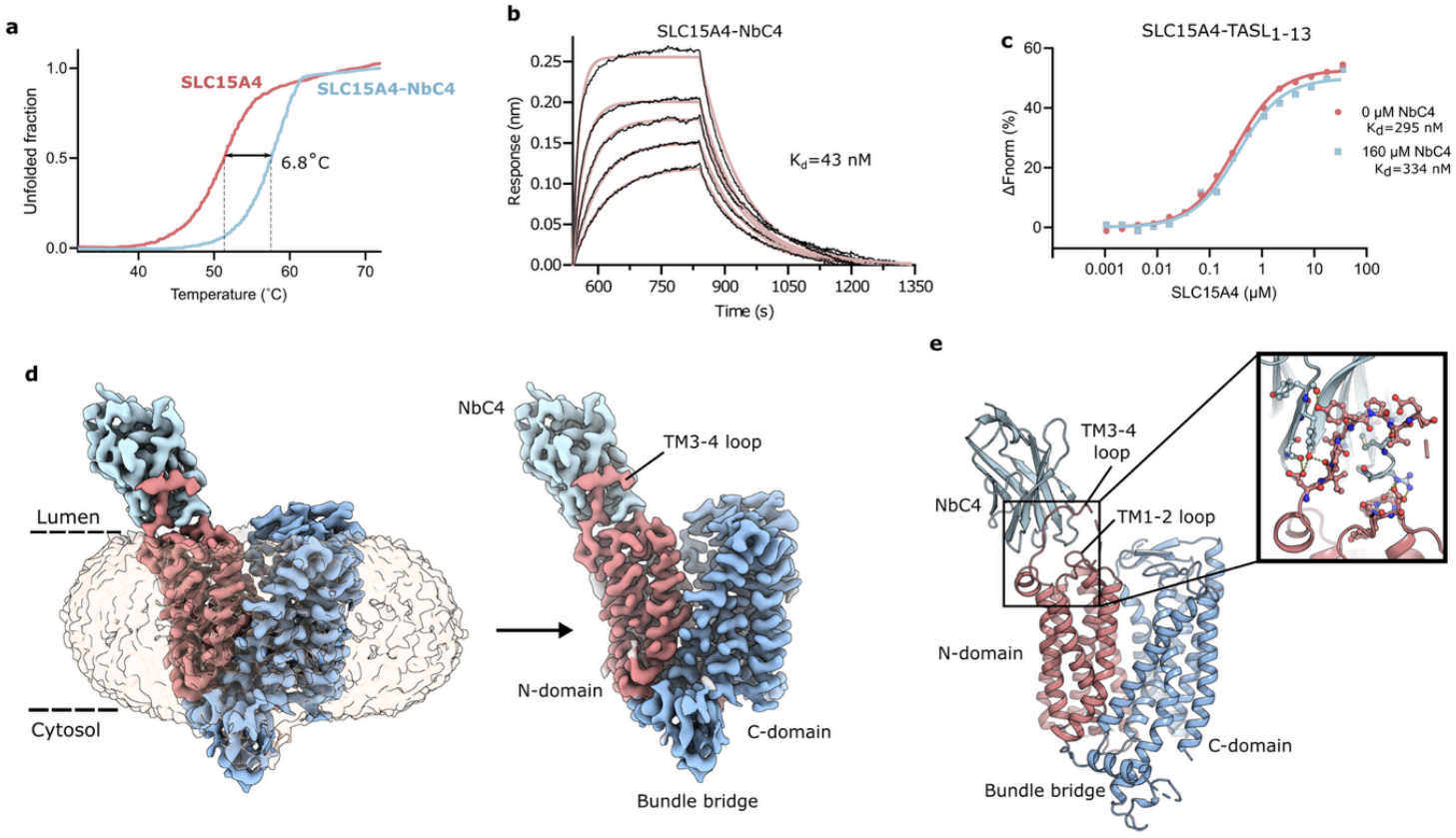


Figure 1

Outward-open structure of SLC15A4 in complex with NbC4

a) nanoDSF unfolding curves of SLC15A4 in the absence (red) and presence (blue) of equimolar NbC4, illustrating a thermal stabilization of ~6.8°C. b) Biolayer interferometry (BLI) sensorgrams of immobilized SLC15A4 titrated with five two-fold dilutions of NbC4 (black traces). Data were fitted with a 1:1 binding model (red lines), yielding K_D = 43 nM (fit error ± 0.41 nM). c) MST binding curves of SLC15A4 with fluorescently labelled TASL$_{1-13}$ peptide in the absence (red, K_D = 295 nM, fit error ± 19 nM) and presence (blue, K_D = 334 nM, fit error ± 39 nM) of 160 μM NbC4, demonstrating that NbC4 does not compete with TASL binding. d) Cryo-EM map of SLC15A4 bound to the conformation non-specific nanobody NbC4. The structure represents the outward-open conformation of SLC15A4 in complex with NbC4 (cyan). NbC4 binds on the luminal side of the N-terminal domain of SLC15A4 (red). The bundle

bridge and the C-terminal domain are shown in blue. e) Cartoon representation of SLC15A4 bound to NbC4 with a close-up view of the nanobody epitope. NbC4 contacts the TM1–2 and TM3–4 luminal loops of the N-terminal bundle.

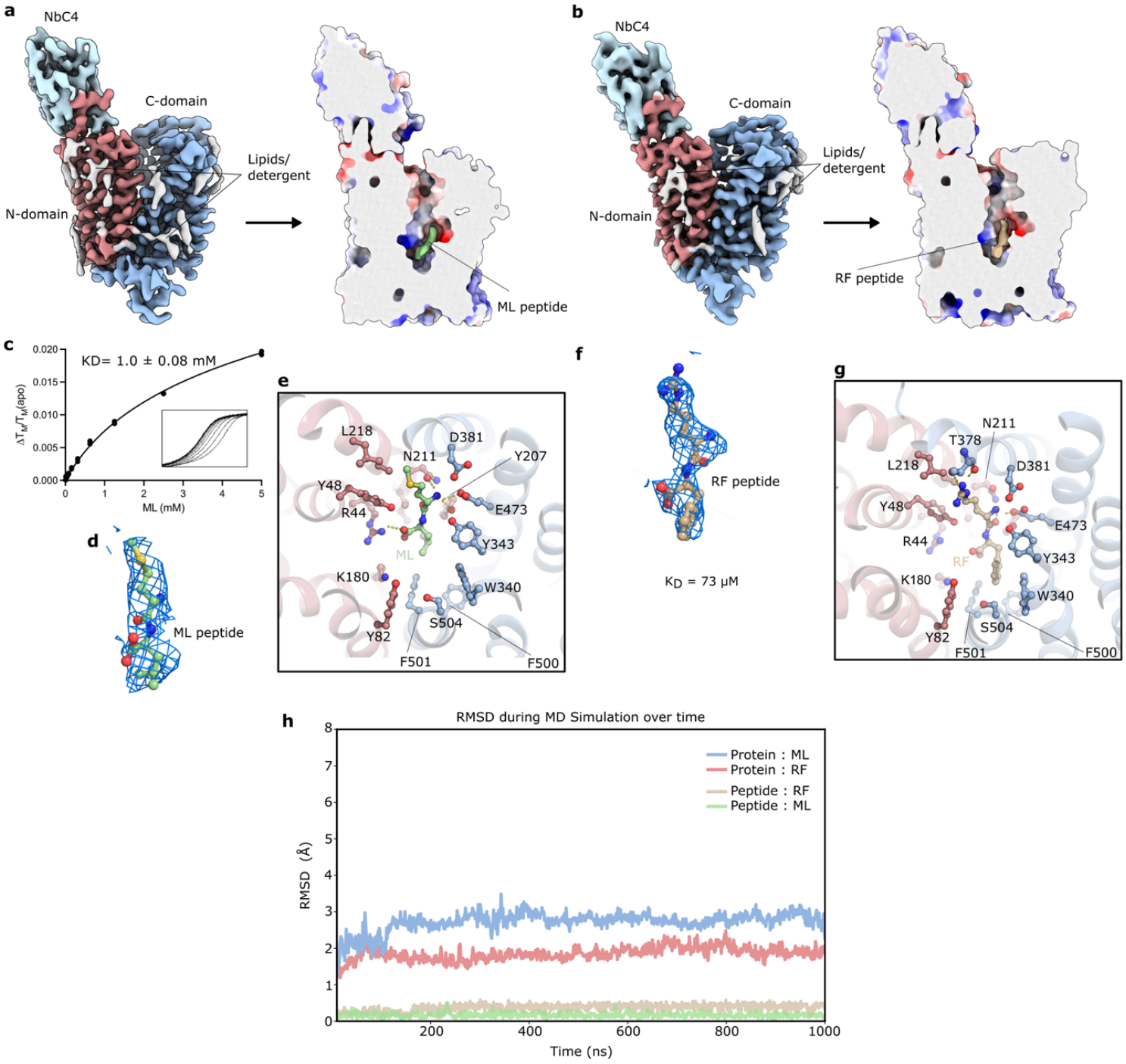


Figure 2

Cryo-EM structures of the SLC15A4-NbC4 complex bound to dipeptides.

Cryo-EM maps of SLC15A4 with NbC4 bound to dipeptides a) ML and b) RF are shown as surface representation and as cross-section of the electrostatic surface. c) Thermal stability changes of

SLC15A4 upon addition of different concentrations of the dipeptide ML. The fit (black continuous line) of these data to a two-state binding model yields the given apparent affinity. Data represent the mean ± SD of two technical replicates. d) Density for the ML dipeptide (green) is illustrated separately at 7s carved within 1.5 Å of the modelled dipeptide. e) The coordination of ML (green) is highlighted in the substrate binding site. Residues of the NTD are shown in red, the ones of the CTD in blue and the peptide in green. Dashes indicate hydrogen bonds (cut-off at 3.5 Å). f) Density for the RF dipeptide (brown) is illustrated separately at 7s carved within 1.5 Å of the modelled dipeptide. g) The coordination of RF (brown) is highlighted in the substrate binding site. Residues of the NTD are shown in red, the ones of the CTD in blue and the peptide in brown. Dashes indicate hydrogen bonds (cut-off at 3.5 Å). h) Root Mean Square Deviation (RMSD) as a function of simulation time for two molecular dynamics (MD) simulations: 1) SLC15A4 bound to the ML peptide and 2) SLC15A4 bound to the RF peptide. RMSD for the peptides is also shown. The RMSD values plateau after an initial equilibration phase, indicating that both systems have reached stability and are equilibrated over the course of the simulations. This suggests that the conformational dynamics of the systems are consistent and reliable for structural analysis.

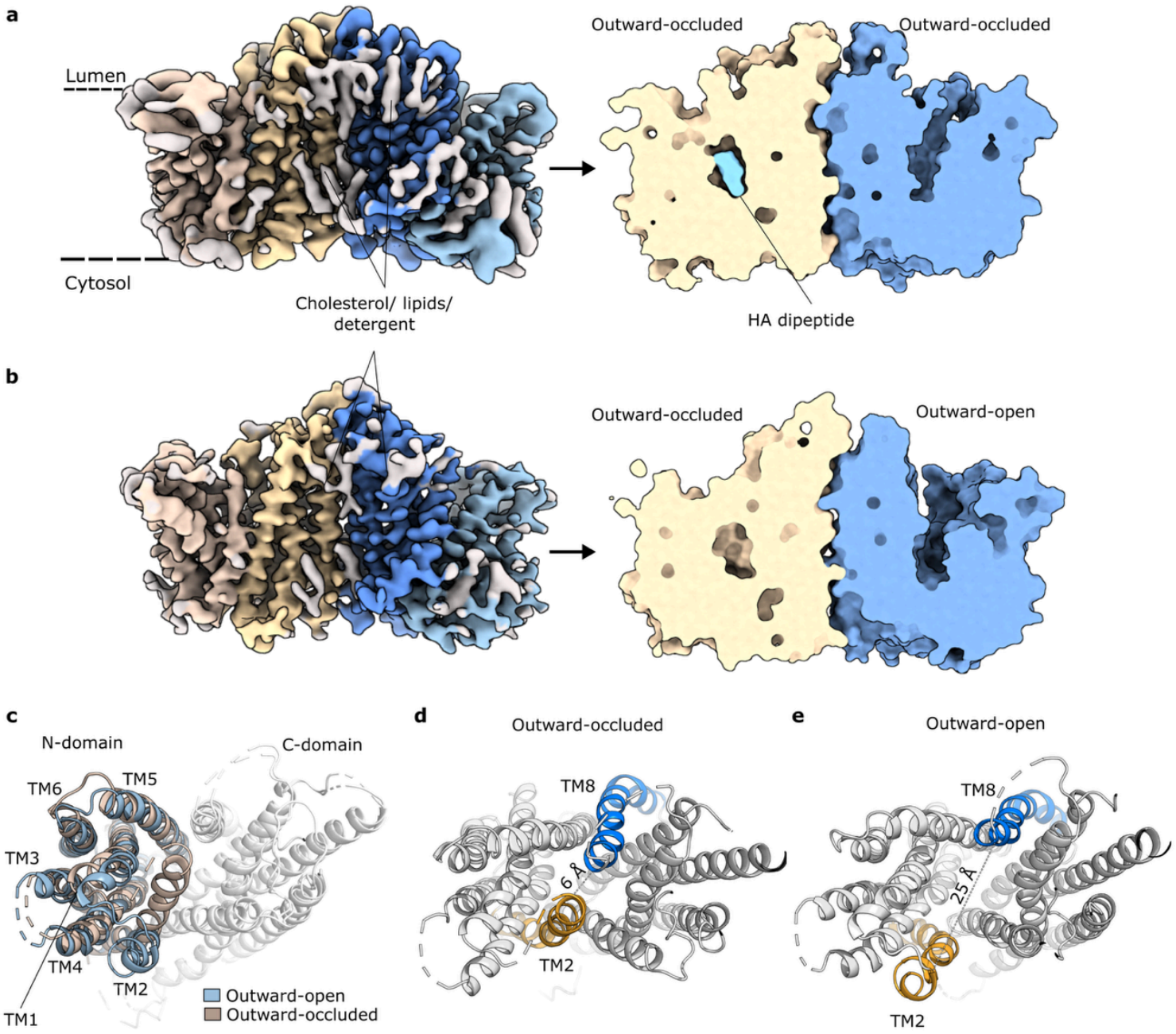


Figure 3

Cryo-EM structures of the SLC15A3 dimer reveal outward-open and outward-occluded conformations. a) Surface representation and cross-section of the cryo-EM map of dimeric SLC15A3 bound to the dipeptide HA (cyan) in one protomer. Both protomers represent an outward-occluded conformation. b) Surface representation and cross-section of the cryo-EM map of dimeric SLC15A3 in its apo form. The protomers display an outward-occluded and outward-open conformation. c) Alignment of outward-open (blue) and outward-occluded (brown) state structures to illustrate conformational changes. For clarity only one protomer is shown and affected TMs are labeled. d-e) Distance measurements between the tips of TM2 and TM8 to highlight the distance changes between both conformations.

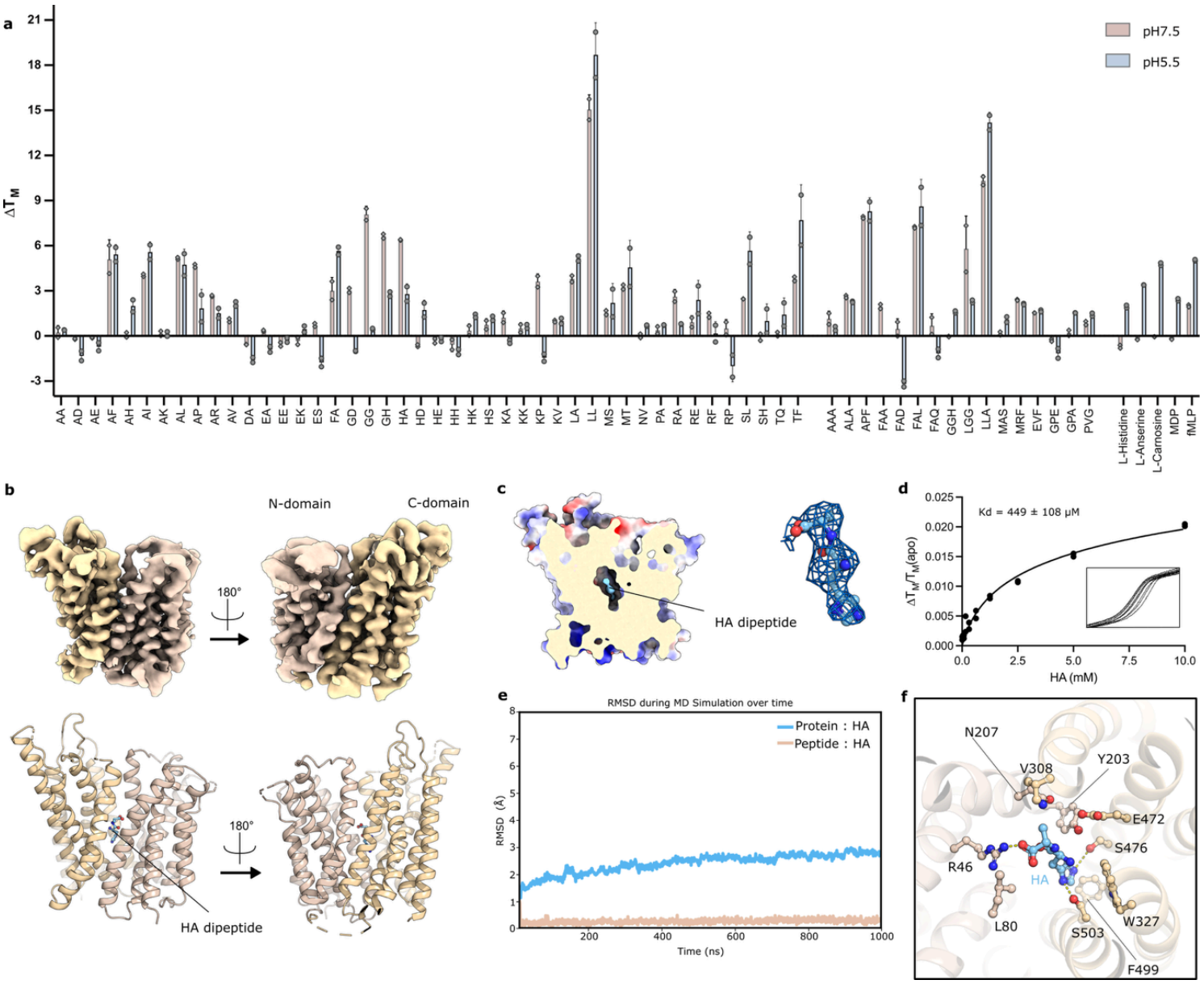


Figure 4

Peptide binding to SLC15A3.

a) Thermal stability of SLC15A3 screened with a ligand library at a concentration of 5 mM at pH 5.5 (blue) and 7.5 (brown). Changes in the melting temperature of SLC15A3 in the presence of a ligand compared to the melting temperature of SLC15A3 alone (ΔT_m) are shown. Library is noted using the 1 letter abbreviation for amino acids. Data represent the mean ± SD of two technical replicates. b) Cryo-EM map (top) and cartoon representation (bottom) of the SLC15A3 protomer bound to the dipeptide HA. c) Cross-section of the electrostatic surface of the SLC15A3 protomer bound to the dipeptide HA. Density for the HA dipeptide (cyan) is illustrated separately at 7s carved within 2 Å of the modelled dipeptide. d) Thermal stability changes of SLC15A3 upon addition of different concentrations of the dipeptide HA. The fit (black continuous line) of these data to a two-state binding model yields the given apparent affinity. e) Root Mean Square Deviation (RMSD) as a function of simulation time for SLC15A3 bound to HA; RMSD

trace for SLC15A3 and the peptide only. f) The coordination of the dipeptide HA (cyan) is highlighted in the substrate binding site. Residues of the N-domain are shown in light red, the ones of the C-domain in yellow and the peptide in cyan. Dashes indicate hydrogen bonds (cut-off at 3.5 Å).

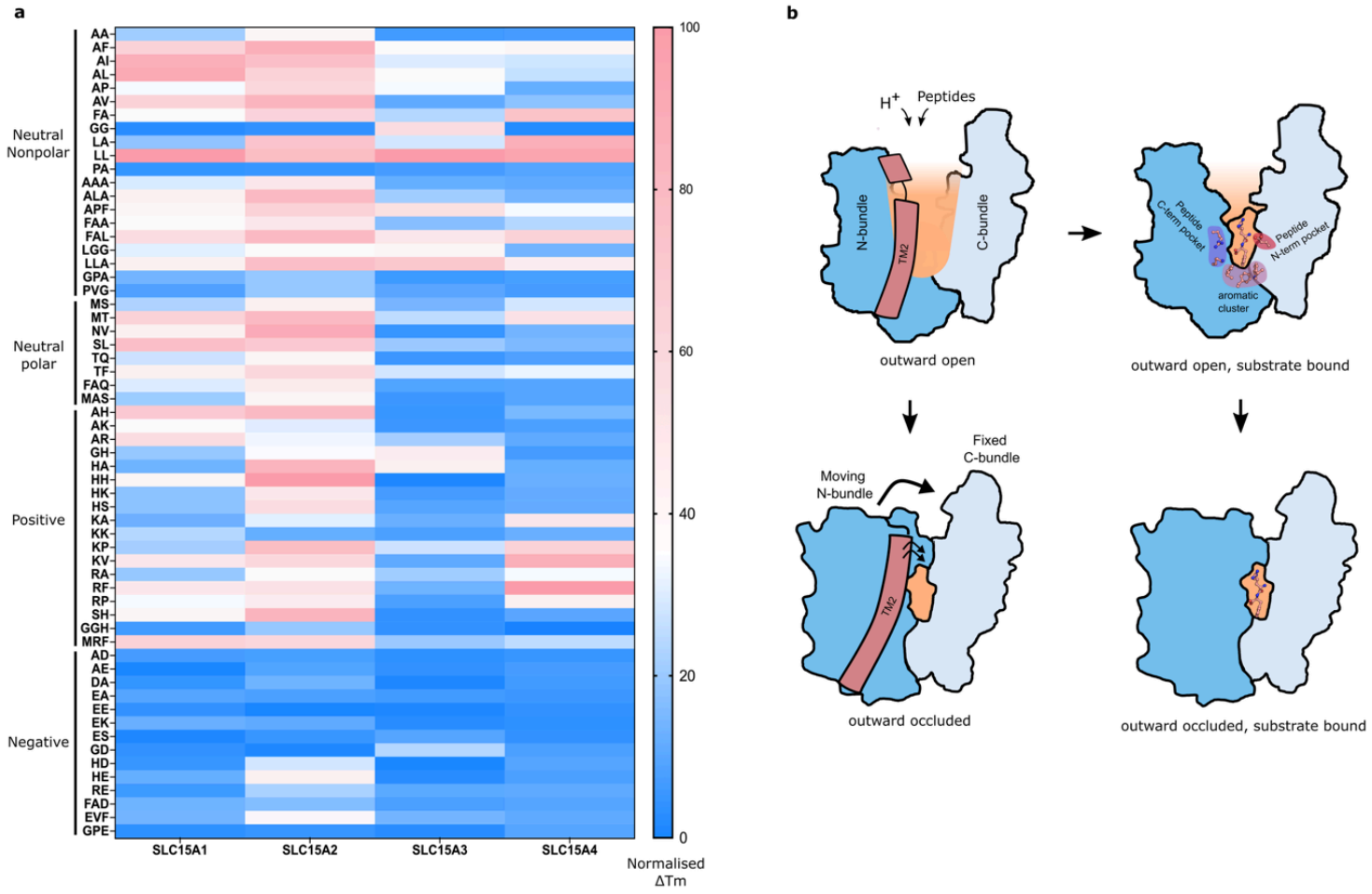


Figure 5

Peptide binding and conformational transitions of SLC15 members.

a) Thermal profiling of the four SLC15 members (SLC15A1=PepT1, SLC15A2=PepT2, SLC15A4 and SLC15A3) against the same di- and tripeptide library at a concentration of 5 mM. The ΔT_m values were normalized independently for each transporter to a scale of 0–100, where 100 corresponds to the strongest stabilization observed for that transporter. Peptides are grouped by side-chain character. b) Schematic of the conformations from the transport cycle captured in this work. A proton and peptide substrate enter from the luminal side; substrate binding is followed by bending of TM2 and inward movement of the N-bundle, which closes the luminal gate resulting in the outward-occluded state, while the C-bundle remains relatively fixed. The pockets coordinating the peptide N- and C-termini are indicated; the peptide N-terminus is bound within the C-bundle and the peptide C-terminus within the N-bundle.

Supplementary Files

This is a list of supplementary files associated with this preprint. Click to download.

- Supplementaryinformation.docx